Optogenetic skeletal muscle-powered adaptive biological machines

Ritu Raman[a,b], Caroline Cvetkovic[b,c], Sebastien G. M. Uzel[d], Randall J. Platt[e], Parijat Sengupta[c,f], Roger D. Kamm[d,e], and Rashid Bashir[b,c,1]

[a]Department of Mechanical Science and Engineering, University of Illinois at Urbana–Champaign, Urbana, IL 61801; [b]Micro and Nanotechnology Laboratory, University of Illinois at Urbana–Champaign, Urbana, IL 61801; [c]Department of Bioengineering, University of Illinois at Urbana–Champaign, Urbana, IL 61801; [d]Department of Mechanical Engineering, Massachusetts Institute of Technology, Cambridge, MA 02139; [e]Department of Biological Engineering, Massachusetts Institute of Technology, Cambridge, MA 02139; and [f]Beckman Institute for Advanced Science and Technology, University of Illinois at Urbana–Champaign, Urbana, IL 61801

Edited by Stephen R. Quake, Stanford University, Stanford, CA, and approved February 11, 2016 (received for review August 13, 2015)

Complex biological systems sense, process, and respond to their surroundings in real time. The ability of such systems to adapt their behavioral response to suit a range of dynamic environmental signals motivates the use of biological materials for other engineering applications. As a step toward forward engineering biological machines (bio-bots) capable of nonnatural functional behaviors, we created a modular light-controlled skeletal muscle-powered bioactuator that can generate up to 300 μN (0.56 kPa) of active tension force in response to a noninvasive optical stimulus. When coupled to a 3D printed flexible bio-bot skeleton, these actuators drive directional locomotion (310 μm/s or 1.3 body lengths/min) and 2D rotational steering (2°/s) in a precisely targeted and controllable manner. The muscle actuators dynamically adapt to their surroundings by adjusting performance in response to "exercise" training stimuli. This demonstration sets the stage for developing multicellular bio-integrated machines and systems for a range of applications.

bioactuator | stereolithography | tissue engineering | soft robotics

Understanding complex biological systems requires uncovering the mechanisms through which integrated multicellular networks accomplish sensing, internal processing, and coordinated action in response to dynamic environmental signals. Attempting to reverse engineer these mechanisms for applications in regenerative medicine has been the focus of the burgeoning field of tissue engineering (1), and seminal advances in this field have targeted nearly every organ system in the body (2). These developments, in addition to improving the state of the art in therapeutics, have furthered our understanding of the design principles governing the organizational structure and function of natural biological systems. With this as a guide, we are ideally poised to start forward engineering biological machines, or bio-bots, capable of complex controllable nonnatural functional behaviors, thereby broadening the potential applications for building with biological materials.

Before we can design bio-integrated machines for a range of applications, we must first engineer modular tissue building blocks that respond to external signals with complex functional behaviors. Observing and controlling the coordinated action of such building blocks in series and parallel will help us understand the emergent behavior of natural biological systems (3, 4). Nearly all machines require actuators, modules that convert energy into motion, to produce a measurable output in response to input stimuli. Efforts to manufacture bio-integrated actuators have targeted a range of cell types (5), including flagellated bacteria (6), cardiac muscle (7–9), and skeletal muscle (10–12). We previously demonstrated a millimeter-scale soft robotic device, or bio-bot, that uses the contractile force produced by electrically paced skeletal muscle to drive locomotion across a substrate (10). This bio-bot was the first demonstration of an untethered locomotive skeletal muscle powered biological machine and set the stage for building hierarchical actuators inspired by natural systems. However, like other previous demonstrations of bio-integrated machines, the actuator was coupled to the surrounding device and did not allow for unrestricted use in a variety of design applications. A significant step forward in this field thus requires a modular bioactuator that demonstrates a variety of controllable and tunable functional behaviors in response to a noninvasive external signal.

Here, we present a bioactuator that can be coupled to many different mechanical bio-bot skeletons to provide a desired contractile force output. Two major design advances enable forward engineering bio-bots capable of more complex behaviors: (*i*) skeletal muscle cells are transduced to express a light sensitive cation channel, using an existing protocol (these optogenetic cells demonstrated controlled contractility in response to noninvasive and spatiotemporally precise optical stimuli); and (*ii*) muscle actuators are redesigned as "rings" that can be readily coupled to a variety of bio-bot skeleton designs. The resulting bioactuators produced paced active tension forces approaching 300 μN per muscle ring. Implementing these rings as the power source in untethered bio-bots enabled directional locomotion at average speeds of 310 μm/s (1.3 body lengths/min) in response to optogenetic stimulation at 2 Hz. The precise spatiotemporal stimulus provided by optogenetic control also enabled the demonstration of rotation and 2D steering in a muscle-powered device, with average rotational speeds of 2°/s (120°/min). Furthermore, "exercise training" of muscle rings with dynamic optical stimuli and static mechanical stimuli during differentiation resulted in a significant increase in functional performance, with generated forces being ∼550% greater in exercised muscle rings compared with a control. These advances in design and

Significance

Understanding the design rules that govern the structure and function of natural biological systems gives us the ability to forward engineer machines integrated with and powered by biological components. Such machines, or "bio-bots," can sense, process, and respond to dynamic environmental signals in real time, enabling a variety of applications. Here we present a modular optogenetic muscle actuator used to power actuation and locomotion of 3D printed flexible skeletons. Observing and controlling the functional response of such muscle-powered machines helps replicate the complex adaptive functionality we observe in natural biological systems. This demonstration thus sets the stage for building the next generation of bio-integrated machines and systems targeted at a diverse array of functional tasks.

Author contributions: R.R. and R.B. designed research; R.R., C.C., and P.S. performed research; R.R., C.C., S.G.M.U., R.J.P., P.S., and R.D.K. contributed new reagents/analytic tools; R.R. analyzed data; and R.R., C.C., S.G.M.U., P.S., R.D.K., and R.B. wrote the paper.

The authors declare no conflict of interest.

This article is a PNAS Direct Submission.

[1]To whom correspondence should be addressed. Email: rbashir@illinois.edu.

This article contains supporting information online at www.pnas.org/lookup/suppl/doi:10.1073/pnas.1516139113/-/DCSupplemental.

implementation of modular muscle actuators thus set the stage for building hierarchical multicellular bio-integrated machines and systems for a range of applications. Primary applications in medicine include noninvasive drug delivery and design of dynamic multifunctional implants.

Results

Design and Fabrication of Optogenetic Muscle Ring-Powered Bio-Bots. In vivo, muscle is anchored to bone via tendons, and the concerted contraction of sarcomeres acting in parallel along a muscle fiber drives articulation of bones across joints. We designed and 3D printed a poly (ethylene glycol) diacrylate (PEGDA) hydrogel skeleton composed of two pillars (artificial tendons) that connect the muscle to a flexible beam (articulating joint) to mimic in vivo structure (Fig. S1*A*). We then 3D printed a PEGDA "ring mold" that served as a template for the formation of a muscle ring. To enable comparisons to our previous muscle strip design (10), we also manufactured a strip mold (Fig. 1*A*).

Optogenetics, the method of genetically engineering light-responsive cells, enables noninvasive external control over cellular function (13). Ion channels that respond to light stimuli have been implemented in a variety of applications that require cellular manipulation. Although the seminal studies in this field were performed on neurons, recent studies have demonstrated optogenetic approaches to control other cell types, including skeletal muscle (12). To implement optogenetic control of our muscle actuators, we used an existing lentiviral transduction protocol to engineer C2C12 murine myoblast cells with a mutated variant of the blue light-sensitive ion channel, Channelrhodopsin-2 (ChR2), namely ChR2(H134R) (Fig. 1*B*). Transduced cells, labeled with a tdTomato tag, were selected using FACS to maximize expression of ChR2(H134R). Multinucleated myotubes differentiated from these myoblasts were anticipated to demonstrate paced contractility in response to an external light stimulus of 470-nm wavelength.

Optogenetic myoblasts were combined with a solution of Matrigel basement membrane, fibrinogen, and thrombin (Fig. 1*C*). This cell/gel solution, designed to mimic native extracellular matrix, was injected into the molds, and traction forces exerted by embedded cells drove self-assembly into densely packed muscle strips and rings (Fig. 1*D*). Muscle strips formed around (and thus were permanently tethered to) the bio-bot skeletons. Muscle rings were manually transferred to bio-bot skeletons 1 d after seeding (day 1) (Fig. 1*E*, Fig. S2, and Movie S1). This process allowed for mechanical coupling of the actuator to the device while still preserving modularity of design, because muscle rings could be transferred to any of a wide variety of mechanical skeletons. To simplify manual transfer, bio-bot skeletons were chemically tethered to an underlying glass slide during transfer and mechanically released from the slide on day 2 after seeding. Both muscle strip and ring devices were cultured in growth medium (DMEM + 10% FBS) containing the fibrinolytic inhibitor aminocaproic acid (ACA) for 3 d to induce cell proliferation. They were then transferred to differentiation medium [DMEM + 10% horse serum (HS)] containing ACA on day 4 to drive fusion of individual myoblasts into multinucleated myotubes with mature contractile sarcomeres. This medium was supplemented with human insulin-like growth factor (IGF1) to accelerate the differentiation process and induce muscle hypertrophy (10, 14).

The thickness of engineered muscle tissue is dependent on the formulation of the cell/gel solution. Until a certain lower limit, higher concentrations of cells and fibrin form thinner muscle rings that lead to more densely compacted tissue. Beyond this limit, increasing the cellular and fibrin concentration cannot reduce the muscle tissue thickness further, as the embedded cells and fibrin network occupy a finite volume. The thickness of muscle rings was thus used as a metric to select cell/gel solution formulations that would maximize muscle tissue compactness and cellular density (Fig. 1*F* and Fig. S3*A*). This characterization of optimal muscle dimensions coupled with the modularity of the ring design enabled forward engineering of many types of machines including larger scale bio-bots, bio-bots powered by multiple muscle rings, and multilegged bio-bots (Fig. S3 *B–D*).

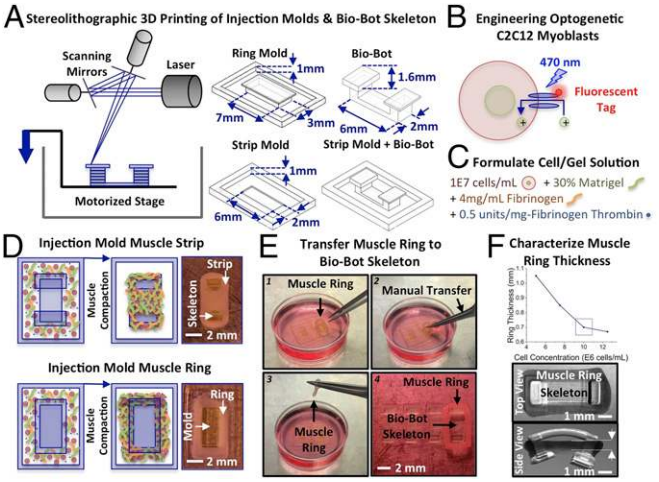

Fig. 1. Design and fabrication of optogenetic muscle ring-powered bio-bots. (*A*) Stereolithographic 3D printing is used to fabricate ring and strip injection molds and bio-bot skeletons from a PEGDA photosensitive resin. (*B*) C2C12 myoblasts are engineered to incorporate a mutant variant of the blue-light sensitive cation channel, Channelrhodopsin-2, in the cell membrane. The ion channel is tagged with a red fluorescent tdTomato tag. (*C*) Optogenetic myoblasts embedded within a natural hydrogel matrix. (*D*) Injection molding of cell/gel solution into muscle strip and ring molds. (*E*) Manual transfer of muscle rings from the injection mold to the bio-bot skeleton (Movie S1). (*F*) Optimization of muscle ring thickness as a function of cell concentration.

Characterization of Optogenetic Muscle Ring Force Output. Macroscale muscle contraction is the sum of many microscale contractions of individual myotubes acting in parallel. Aligning the axis of contractility for myotubes within muscle is thus critical to observing large combined forces. We performed immunofluorescence staining on muscle rings to observe the distribution of the mature muscle marker, myosin motor protein. A fast Fourier transform (FFT) algorithm was used to determine local alignment (Fig. 2*A*). Myotubes in muscle rings are aligned at 90° in regions parallel to the bio-bot beam (Fig. 2*A-1*) and shift in alignment around the edges of the skeleton with smaller peaks at 90° and a larger peaks at 45° (Fig. 2*A-2*) and 135° (Fig. 2*A-3*), respectively. This analysis reveals a high degree of local alignment along the axis of tension imposed by the mechanical constraint of the bio-bot skeleton.

We performed a closer inspection of muscle ring architecture in the region represented in Fig. 2*A-2* via multichannel fluorescence imaging of DAPI cell nucleus marker, the ChR2 tdTomato tag, and the immunostained myosin marker (Fig. 2*B*). Cells were evenly distributed throughout the muscle ring and expressed the tdTomato marker for optogenetic ion channels, indicating that they could be expected to generate functional contractile responses to blue light stimulation. Scanning electron microscopy imaging likewise showed densely compacted and evenly distributed myotubes with a high degree of local alignment (Fig. 2*C*). A cross-section image of the muscle ring was used to verify that hierarchical organization of muscle architecture and alignment was preserved in 3D (Fig. 2*D*).

To measure the passive tension force exerted by both muscle strip and muscle ring devices, we used Euler-Bernoulli beam bending theory to correlate bio-bot skeleton deformation with muscle force production. On average, passive tension forces for muscle strip and ring devices were not significantly different, with muscle strips exerting passive tension forces of 1,940 ±

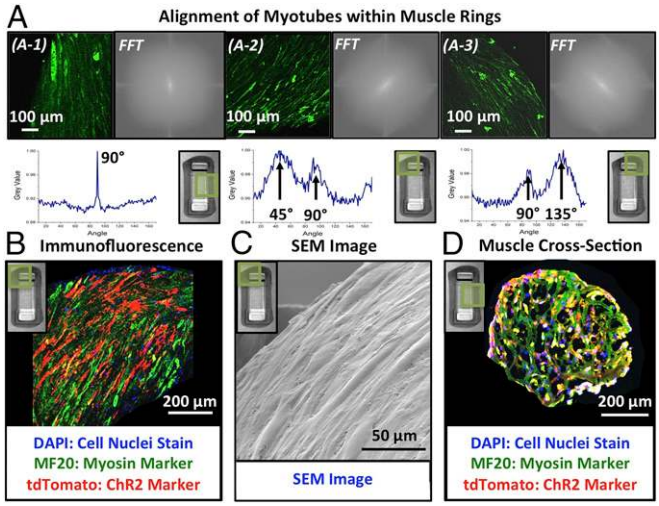

Fig. 2. Characterization of muscle ring architecture. (*A*) Alignment of myotubes within various regions of muscle rings assessed via FFT analysis of fluorescent myosin marker. Fluorescence image (*Upper Left*), FFT (*Upper Right*), and normalized gray value of the FFT as a function of angle (*Lower Left*) are presented for three regions of muscle rings, shown as green highlights on a whole device (*Lower Right*). (*B*) Multichannel fluorescence imaging of DAPI cell nucleus marker, the optogenetic ChR2 tdTomato tag, and the MF-20 myosin marker imaged via confocal fluorescence microscopy and presented as a merged 3D stack. (*C*) Scanning electron microscopy image of muscle ring surface. (*D*) Cross-section of fluorescent immunostained muscle ring, showing uniform distribution of mature functional myotubes throughout the entire cross-section.

350 µN and muscle rings exerting passive tension forces of 1,710 ± 230 µN on day 9 after seeding (Fig. S4*A*). This force corresponds to a passive tension stress of 1.6 ± 0.3 kPa for muscle strips, which had average cross-sectional areas of 1.2 ± 0.04 mm^2 ($n = 3$), and 3.2 ± 0.4 kPa for muscle rings, which had had average cross-sectional areas of 0.54 ± 0.06 mm^2 ($n = 3$). These stress values are comparable to those previously reported for tissue engineered skeletal muscle (10, 12, 15).

Mature muscle was stimulated optically and electrically using custom-built apparatus (Fig. 3*A*), and a Kelvin-Voigt viscoelasticity model was used to correlate contraction-induced displacement of bio-bot skeletons to active tension forces produced by engineered muscle. Optical stimulation of muscle strip and ring devices at 1, 2, and 4 Hz with 50-ms pulses produced paced contractions (Fig. S4*B*) and physiological force-frequency response behavior (Fig. 3 *B-1* and *C-1*), where the dynamic fluctuation of active tension force reduced with increasing frequency. As with native skeletal muscle at high frequency stimulation, the passive tension baseline increased during the stimulation period, indicating that the muscle was not allowed to fully relax from one received stimulus before the next received stimulus. For muscle strips, forces produced by optical stimulation (45 ± 11, 32 ± 12, and 25 ± 12 µN at 1, 2, and 4 Hz, respectively) are significantly lower (Fig. 3*B-2*) than those produced by electrical stimulation (195 ± 19, 112 ± 26, and 88 ± 30 µN at 1, 2, and 4 Hz, respectively). By contrast, there was no significant difference between optical and electrically stimulated active tension forces in muscle rings (Fig. 3*C-2*). At stimulation frequencies of 1, 2, and 4 Hz, optical stimulation of rings produced active tension forces of 195 ± 7.3, 114 ± 8.1, and 110 ± 16 µN, respectively, whereas electrical stimulation produced active tension forces of 185 ± 17, 117 ± 19, and 119 ± 6.7 µN.

This difference in functional performance of optogenetic muscle strips and rings is explained by an analysis of the effective penetration depth (500–740 µm) of 470-nm light into biological tissue (16, 17). Although muscle strips had maximum thicknesses up to 1,200 µm, the densely compacted muscle ring actuators were less than 700 µm thick (Fig. 1*D*). Hence, light stimulation of muscle rings excited a larger number of myotubes than in muscle strips, resulting in greater force production. This principle was verified by demonstrating that increasing light energy density increased muscle ring functional performance (Fig. S4*C*). A maximum energy density of 1.9 mW/mm^2 was used for all experiments, a value that falls within the range of saturation intensity values reported in the literature on optogenetic cells (12, 18, 19). Electrical stimulation of muscle strips and rings revealed comparable active tension force production for both designs, indicating that similar numbers of myotubes were recruited in each case (Fig. S4*D*). When normalized by cross-sectional area, however, muscle rings produced significantly greater active

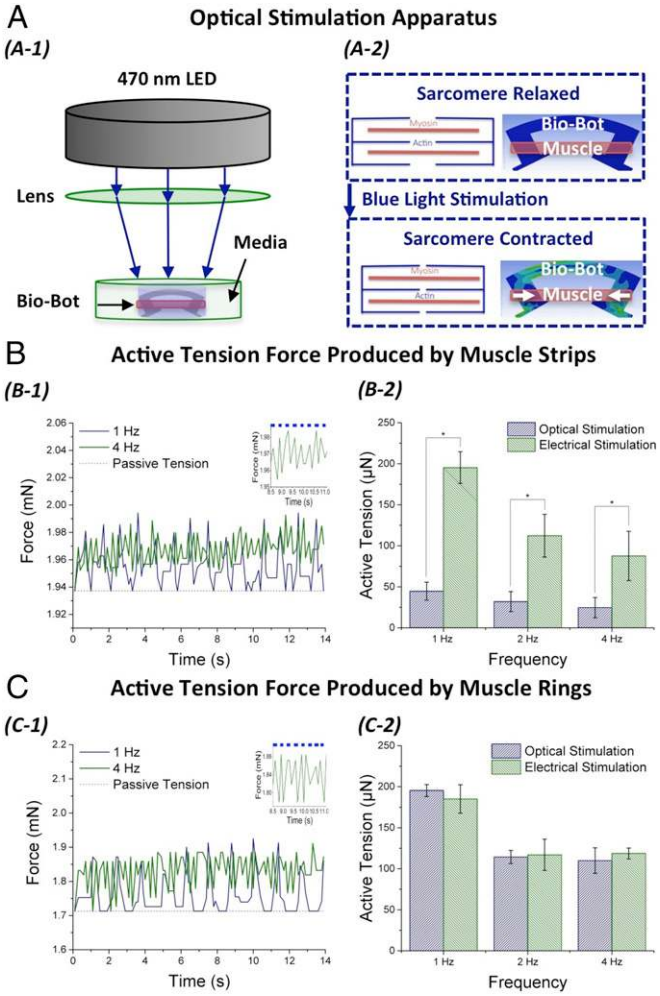

Fig. 3. Optically stimulated actuation of muscle strips and rings. (*A*) Apparatus used to optically stimulate engineered muscle. (*A-1*) 470-nm light is focused on to bio-bots at a maximum intensity of 1.9 mW/mm^2. (*A-2*) At the microscale, light stimulation induces contraction of individual myotubes. The coordinated contraction of several sarcomeres produces observable macroscale contraction. (*B*) Active tension force produced by muscle strips (day 12). (*B-1*) Active tension force tracked over time for a representative muscle strip. *Inset* of 4-Hz stimulation over 2 s shown for clarity, with a dashed blue line indicating the stimulus pulse train. (*B-2*) Active tension force compared between optical and electrical stimulation of muscle strips ($P < 0.05$, $n = 3$, one-way ANOVA, post hoc Tukey test). (*C*) Active tension force produced by muscle rings (day 12). (*C-1*) Active tension force tracked over time for a representative muscle ring. *Inset* of 4-Hz stimulation over 2 s shown for clarity, with a dashed blue line indicating the stimulus pulse train. (*C-2*) Active tension force compared between optical and electrical stimulation of muscle rings ($P < 0.05$, $n = 3$, one-way ANOVA, post hoc Tukey test). All data are presented as mean ± SD.

tension stresses with a maximum of 0.34 ± 0.03 kPa at 1-Hz stimulation compared with muscle strips, which produced active tension stresses of only 0.16 ± 0.02 kPa.

Optimizing Functional Performance of Optogenetic Muscle Rings. "Exercise training" of engineered muscle during differentiation has been shown to increase force output. For electrically stimulated conditioning, improved functionality is attributed to increased differentiation, improved alignment, and increased glucose uptake (20, 21). For mechanically stimulated conditioning, improved functionality is attributed to a change in gene regulation and protein expression, increased metabolic activity, cellular proliferation, and improved myofiber organization (10, 22).

A previous study has shown that optical stimulation during differentiation of optogenetic C2C12s in 2D can improve the alignment of sarcomeric proteins and increase the fraction of contractile myotubes (23). We hypothesized that optical conditioning of muscle rings during differentiation could thus lead to an enhancement in functional performance (force production). The mechanism of periodic cellular depolarization and contraction would be similar to that of electrical stimulation, but less invasive, as it avoids electrolysis of the surrounding media. Furthermore, we hypothesized that combining mechanical and optical stimulation could lead to synergistic enhancements in functional performance.

To provide a passive mechanical stimulus during differentiation, we kept bio-bots chemically tethered to an underlying glass slide throughout differentiation to maximize cellular alignment and myotube formation. Bio-bots were mechanically released from the stiff underlying substrate before stimulation. To provide optical conditioning during differentiation, we subjected muscle rings to a daily regimen of optical stimulation at 1, 2, and 4 Hz. We measured active tension force output for four different groups: control group 1, no mechanical conditioning (bio-bots released from substrate on day 1), no optical conditioning; control group 2, mechanical conditioning (bio-bots tethered to substrate until day 12), no optical conditioning; exercise group 1, no mechanical conditioning, optical conditioning during differentiation (days 4–11); and exercise group 2, mechanical conditioning, optical conditioning (Fig. 4*A*).

An analysis of force output for exercise group 1 revealed that active tension forces grew from 56 ± 11 μN on day 7 (the first day with observable macroscale contractility) to 195 ± 24 μN on day 12 at 1-Hz stimulation (Fig. 4*B-1*). By contrast, control group 1 produced active tension forces of only 43 ± 6.0 μN on day 12. Control group 2 produced forces of 91 ± 37 μN on day 12. Although these forces were higher than those of bio-bots from control group 1, the results were not significantly different. Exercise group 2, which was subjected to both mechanical and optically stimulated exercise during differentiation, produced active tension forces of 283 ± 32 μN on day 12 (Fig. 4*B-2* and Movie S2). These data serve to demonstrate that mechanically and optically stimulated exercise can lead to significant improvements in muscle functional performance, and the combination of both types of stimuli synergistically enhances force output even further. This result is consistent with previous demonstrations of mechanical and electrical multimodal stimulation for engineered muscle (24, 25) but is the first demonstration, to our knowledge, of optical conditioning driving functional improvements in muscle performance. As optical stimulation provides a less invasive and cell type-specific approach for localized control of muscle contraction, this approach to enhancing functional performance is a significant improvement over the current state of the art.

To validate our hypothesis that optical stimulus conditioning improves myotube formation, we assessed the DNA and protein content in control group 2 and exercise group 2 muscle rings and compared the ratio of protein/DNA in each case. Larger protein/DNA ratios are correlated with greater cellular hypertrophy (15). As all rings contained the same number of embedded myoblasts, the DNA content for all muscle rings was 1.76 ± 0.35 μg DNA/mg muscle. However, the protein content for exercise group 2 rings

A **Exercise Stimulation Regimen**

Day	Control Group 1	Control Group 2	Exercise Group 1	Exercise Group 2
1-3	No Optical or Mechanical Stimulation	No Optical Stimulation	No Optical or Mechanical Stimulation	No Optical Stimulation
4-11	No Optical or Mechanical Stimulation	No Optical Stimulation	Optical Stimulation: 1 Hz (5 min) 2 Hz (5 min) 4 Hz (5 min) No Mechanical Stimulation	Optical Stimulation: 1 Hz (5 min) 2 Hz (5 min) 4 Hz (5 min)
12	Optical Stimulation	Optical Stimulation	Optical Stimulation	Optical Stimulation

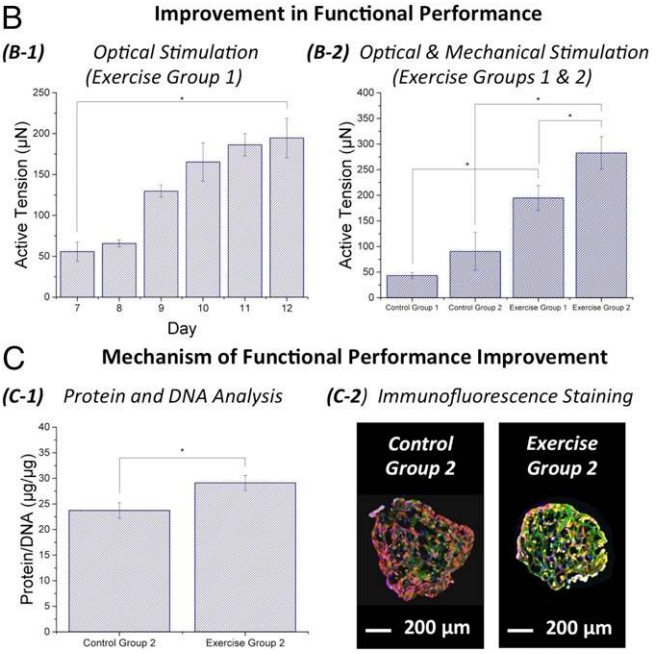

Fig. 4. Functional performance optimization via exercise training. (*A*) Exercise stimulation regimen for four experimental groups during growth (days 1–3) and differentiation (days 4–11) (Fig. S2). Force output in response to optical stimulation is compared on day 12. (*B*) Improvement of muscle functional performance in response to optical conditioning. (*B-1*) Active tension produced by exercise group 1 assessed from days 7 to 12 ($P < 0.05$, $n = 3$, one-way ANOVA, post hoc Tukey test). (*B-2*) Active tension comparison between all four experimental groups (Movie S2) ($P < 0.05$, $n = 3$, one-way ANOVA, post hoc Tukey test). (*C*) Assessment of mechanisms underlying functional performance improvement. (*C-1*) Ratio of protein content to DNA content measured for control group 2 and exercise group 2 ($P < 0.05$, $n = 4$, one-way ANOVA, post hoc Tukey test). (*C-2*) Immunofluorescence stained cross-sections of exercise group 2 and control group 2, showing visibly greater expression of myosin marker in exercised muscle rings. All data are presented as mean ± SD.

was 51.2 ± 2.6 μg protein/mg muscle, compared with 41.7 ± 2.7 μg protein/mg muscle for control group 2. The ratio of protein/DNA was thus significantly larger in the exercise conditioned case, 29.1 ± 1.5 μg protein/μg DNA compared with the control group, 23.7 ± 1.5 μg protein/μg DNA, corroborating the theory that exercise conditioning resulted in increased cellular hypertrophy (Fig. 4*C*).

Directional Locomotion and 2D Steering in Optogenetic Muscle Ring-Powered Bio-Bots. Because the most readily observable form of work produced by an actuator is locomotion, this was chosen as the desired functional output for our muscle-powered machines. First, to observe directional (1D) locomotion in response to optical stimulation, the design of the bio-bot skeleton was made asymmetric by increasing the length of one of the hydrogel pillars. With each contraction of the engineered muscle tissue, the

longer pillar displaced a greater amount than the shorter pillar, as the "moment arm" from the muscle to the beam was greater. This difference in displacement drove net movement in the direction of the longer pillar (Fig. 5*A* and Movie S3). This inch worm-like walking was readily observed and measured, allowing for a simple method of assessing bio-bot functional performance. A comparison of bio-bot speed for the muscle rings in the exercise training study revealed that rings in exercise group 2 powered walking at speeds of 138 ± 6.4 μm/s (optical stimulation, 1 Hz) and 145 ± 19 μm/s (electrical stimulation, 1 Hz). By contrast, rings in control group 2 powered walking at significantly slower speeds of 35 ± 8.5 μm/s (optical stimulation, 1 Hz) and 38 ± 5.1 μm/s (electrical stimulation, 1 Hz) (Fig. 5*B*). Increasing the frequency of stimulation correspondingly increased locomotive speed, despite the reduction in the dynamic range of active tension at higher frequencies. Bio-bot speed increased nearly 80% from 138 ± 6.4 μm/s at 1 Hz to 246 ± 59 μm/s to 4 Hz, providing an added mechanism of improving and controlling performance (Fig. 5*C*).

The true advantage of incorporating optogenetics is the precision stimulation enabled by enhanced spatial control. Focusing light onto different regions of the muscle ring enables control over the number and location of excited myotubes and hence control over the magnitude and direction of macroscale force output. Directional locomotion in 1D and steering in 2D can thus be induced and controlled via the external stimulus without requiring asymmetric modifications to the physical geometry of the bio-bot device itself. To provide a simple demonstration of this design principle, we took advantage of the modularity of the muscle ring actuators to design a two-leg geometrically symmetric skeleton powered by a muscle ring actuator tethered to each leg (Fig. S1*B*). Finite element analysis (FEA) simulations predicted that stimulation of both muscle rings at the same time would result in zero net movement, due to overall symmetry of pillar displacement (Fig. 6*A-1* and Movie S4). This prediction was verified by electrical stimulation of a two-leg bio-bot device, which demonstrated paced contractility but zero net locomotion in response to whole device stimulation at 2 Hz (Fig. 6*A-2* and Movie S5). FEA simulations also predicted that stimulation of only one muscle ring would drive directional locomotion in the direction of the stimulated leg (Fig. 6*B-1* and Movie S6). Optical stimulation of only one leg, for the same bio-bot device electrically stimulated in Fig. 6*A-2*, resulted in net locomotion in the direction of the stimulated leg at speeds of up to 310 μm/s (1.3 body lengths/min) at 2-Hz stimulation (Fig. 6*B-2* and Movie S7). Furthermore, exciting only half of a muscle ring with a light stimulus resulted in rotational locomotion as predicted by FEA (Fig. 6*C-1* and Movie S8) and verified empirically (for the same bio-bot device shown in Fig. 6 *A-2* and *B-2*) at 2.25°/s (135°/min) at 2-Hz stimulation (Fig. 6*C-2* and Movie S9). These results, presented for a single representative bio-bot, indicate that the demonstrated differences in locomotive behavior for this device

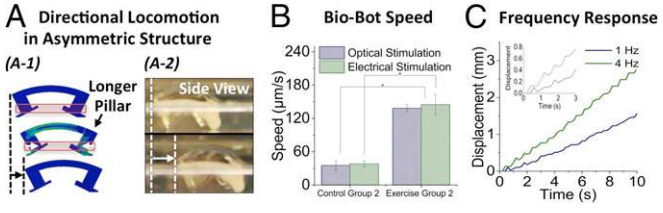

Fig. 5. Optically stimulated 1D locomotion. (*A*) Directional locomotion of optogenetic muscle ring powered bio-bots shown as a schematic (*A-1*) and time lapse images from a movie (*A-2*) (Movie S3). (*B*) Assessment of bio-bot speed from control group 2 and exercise group 2 in response to optical and electrical stimulation at 1 Hz ($P < 0.05$, $n = 3$, one-way ANOVA, post hoc Tukey test). (*C*) Speed-frequency response of bio-bots at 1 and 4 Hz. *Inset* shows displacement over a 3-s time period for clarity. All data are presented as mean ± SD.

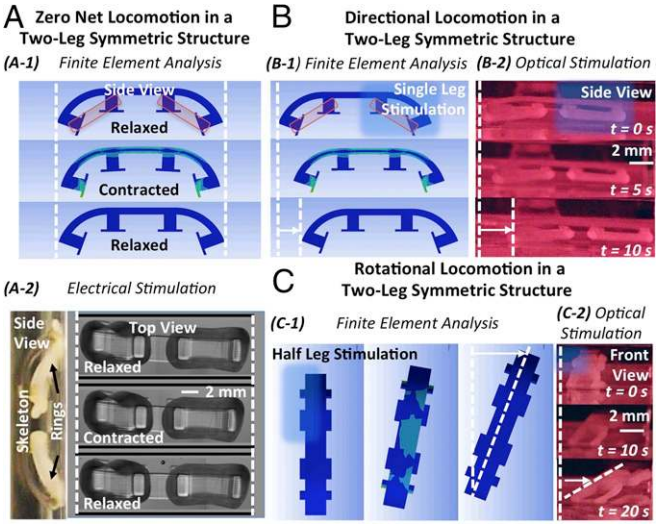

Fig. 6. Optically stimulated 2D locomotion and steering. (*A*) Whole device stimulation of a geometrically symmetric two-leg bio-bot shows zero net locomotion predicted via FEA (*A-1*; Movie S4) and confirmed via electrical stimulation (*A-2*; Movie S5). Side view image of two-leg device shown for clarity. (*B*) Single leg stimulation of a geometrically symmetric structure drives locomotion in the direction of the stimulated leg predicted via FEA (*B-1*; Movie S6) and confirmed via optical stimulation for the same device presented in *A-2* (*B-2*; Movie S7). (*C*) Half of a single leg in a geometrically symmetric structure is stimulated to drive rotational locomotion, as predicted via FEA (*C-1*; Movie S8) and confirmed via optical stimulation for the same device presented in *A-2* and *B-2* (*C-2*; Movie S9). Statistical analyses of multiple two-legged bio-bots is presented in Fig. S5.

can be attributed purely to the mode of external stimulation (both rings, one ring, half ring).

On average, two-legged bio-bots conditioned using the regimen specified for exercise group 2 demonstrated directional locomotion (in response to one ring stimulation) at 312 ± 63 μm/s at 2 Hz (Fig. S5*A-1*), significantly greater than control group 2 two-leg bio-bots, which demonstrated speeds of only 97.5 ± 16 μm/s at 2 Hz (Fig. S5*A-2*). The same exercise group and control group two-legged bio-bots were tested with half ring stimulation at 2 Hz, to show that differential responses could be obtained by changing the mode of external stimulation (Fig. S5*B*). Exercised bio-bots demonstrated rotational locomotion at 2.1 ± 0.5°/s, significantly greater than the control bio-bots, which demonstrated rotational locomotion at speeds of 0.95 ± 0.2°/s. In future, a moving light stimulus that combines whole and partial ring stimulation could be used to direct and drive both directional locomotion and 2D steering of symmetric bio-bot devices in a precisely controlled manner.

Discussion

Here we presented a controllable and modular bioactuator that can be readily adapted to a variety of device designs and applications. Although locomotion is presented as the desired functional output in this study, muscle rings produce significant contractile force output even when untethered to a mechanical skeleton (Movie S10). Such rings can thus be combined in parallel and series to fabricate pumps, swimmers, etc., in future designs that harness the modularity of this technology, proving to be more reproducible and widely adaptable than the bioactuators originally presented as proof-of-concept studies. Using the well-defined characterization of ring composition, dimensions, and modulated force output, we can now treat engineered muscle rings, or rings formed from other cell types, as "building blocks" that enable the fabrication of complex multicellular biointegrated machines and systems.

Incorporating optogenetic ion channels into muscle rings provided us with a noninvasive method of exciting groups of aligned myotubes with precise spatiotemporal control. Compared with previously presented approaches, which controlled muscle-powered bioactuators via electrodes in close proximity to the bioactuator device, optogenetics provided noncontact yet localized control of stimulation. This fundamental distinction drove complex controllable directional locomotion and 2D steering of bio-bots, a capability that has not been previously presented in untethered biological machines powered by engineered muscle. This design modification, enabled by targeted genetic engineering of skeletal muscle myoblasts, thus resulted in a profound improvement in the complexity of functional behaviors produced by engineered muscle. An important advancement presented in this study is the improvement in functional performance produced by exercise training of muscle rings with combined optical and mechanical stimuli. This evidence of increased muscle force production in response to multimodal conditioning demonstrates the dynamically tunable and adaptive nature of these modular bioactuators.

Conclusions

Forward engineered biological machines harness the ability of biological materials to sense, process, and respond to environmental signals in real time. The modular bioactuators we present in this study power bio-bots that demonstrate adaptive behavior in response to noninvasive light stimuli, enabling a variety of applications that require dynamic sensing and actuation. This type of adaptive behavior, which emerges from the coordinated interactions in a multicellular network, drives much of the complex functionality we observe in natural biological systems (26). Future generations of bio-bots could further harness the power of biological materials by incorporating self-assembling or self-healing functionalities or serving as factories of cell-secreted factors. Incorporating multiple cell types, such as neurons for signal processing or endothelial cells for vascularization and nutrient transport, would enable the design and fabrication of more complex biological machines. As many such machines will require modular bioactuators, this demonstration of a light-controlled adaptive skeletal muscle-powered biological machine thus enables a variety of applications while simultaneously setting the stage for the next generation of bio-integrated machines and systems.

Methods

Information on design and fabrication of 3D printed optogenetic muscle-powered bio-bots and quantification of functional performance all appear in *SI Methods*.

ACKNOWLEDGMENTS. We thank Prof. Taher Saif and Brian Williams from University of Illinois at Urbana–Champaign (UIUC) and Prof. H. Harry Asada from Massachusetts Institute of Technology for technical discussions, and Dr. Mayandi Sivaguru from UIUC for assistance with confocal imaging. This work was funded by National Science Foundation (NSF) Science and Technology Center Emergent Behavior of Integrated Cellular Systems (EBICS) Grant CBET-0939511. R.R. was funded by NSF Graduate Research Fellowship Grant DGE-1144245 and NSF Cellular and Molecular Mechanics and Bionanotechnology (CMMB) Integrative Graduate Education and Research Traineeship (IGERT) at UIUC (Grant 0965918).

1. Griffith LG, Naughton G (2002) Tissue engineering—Current challenges and expanding opportunities. *Science* 295(5557):1009–1014.
2. Harrison RH, St-Pierre J-P, Stevens MM (2014) Tissue engineering and regenerative medicine: A year in review. *Tissue Eng Part B Rev* 20(1):1–16.
3. Kamm RD, Bashir R (2014) Creating living cellular machines. *Ann Biomed Eng* 42(2): 445–459.
4. Egan P, Moore J, Schunn C, Cagan J, LeDuc P (2015) Emergent systems energy laws for predicting myosin ensemble processivity. *PLOS Comput Biol* 11(4):e1004177.
5. Chan V, Asada HH, Bashir R (2014) Utilization and control of bioactuators across multiple length scales. *Lab Chip* 14(4):653–670.
6. Carlsen RW, Edwards MR, Zhuang J, Pacoret C, Sitti M (2014) Magnetic steering control of multi-cellular bio-hybrid microswimmers. *Lab Chip* 14(19):3850–3859.
7. Feinberg AW, et al. (2007) Muscular thin films for building actuators and powering devices. *Science* 317(5843):1366–1370.
8. Nawroth JC, et al. (2012) A tissue-engineered jellyfish with biomimetic propulsion. *Nat Biotechnol* 30(8):792–797.
9. Chan V, et al. (2012) Development of miniaturized walking biological machines. *Sci Rep* 2:857.
10. Cvetkovic C, et al. (2014) Three-dimensionally printed biological machines powered by skeletal muscle. *Proc Natl Acad Sci USA* 111(28):10125–10130.
11. Neal D, Sakar MS, Ong L-LS, Harry Asada H (2014) Formation of elongated fascicle-inspired 3D tissues consisting of high-density, aligned cells using sacrificial outer molding. *Lab Chip* 14(11):1907–1916.
12. Sakar MS, et al. (2012) Formation and optogenetic control of engineered 3D skeletal muscle bioactuators. *Lab Chip* 12(23):4976–4985.
13. Deisseroth K (2011) Optogenetics. *Nat Methods* 8(1):26–29.
14. Vandenburgh HH, Karlisch P, Shansky J, Feldstein R (1991) Insulin and IGF-I induce pronounced hypertrophy of skeletal myofibers in tissue culture. *Am J Physiol* 260(3 Pt 1):C475–C484.
15. Hinds S, Bian W, Dennis RG, Bursac N (2011) The role of extracellular matrix composition in structure and function of bioengineered skeletal muscle. *Biomaterials* 32(14):3575–3583.
16. Barolet D (2008) Light-emitting diodes (LEDs) in dermatology. *Semin Cutan Med Surg* 27(4):227–238.
17. Moreira MC, Prado R, Campos A (2011) Application of high brightness LEDs in the human tissue and its therapeutic response. *Applied Biomedical Engineering*, eds Gargiulo GD, McEwan A (InTech, Rijeka, Croatia), pp 3–20.
18. Klapoetke NC, et al. (2014) Independent optical excitation of distinct neural populations. *Nat Methods* 11(3):338–346.
19. Bryson JB, et al. (2014) Optical control of muscle function by transplantation of stem cell-derived motor neurons in mice. *Science* 344(6179):94–97.
20. Duffy RM, Feinberg AW (2014) Engineered skeletal muscle tissue for soft robotics: Fabrication strategies, current applications, and future challenges. *Wiley Interdiscip Rev Nanomed Nanobiotechnol* 6(2):178–195.
21. Donnelly K, et al. (2010) A novel bioreactor for stimulating skeletal muscle in vitro. *Tissue Eng Part C Methods* 16(4):711–718.
22. Powell CA, Smiley BL, Mills J, Vandenburgh HH (2002) Mechanical stimulation improves tissue-engineered human skeletal muscle. *Am J Physiol Cell Physiol* 283(5): C1557–C1565.
23. Asano T, Ishizuka T, Morishima K, Yawo H (2015) Optogenetic induction of contractile ability in immature C2C12 myotubes. *Sci Rep* 5:8317.
24. Rangarajan S, Madden L, Bursac N (2014) Use of flow, electrical, and mechanical stimulation to promote engineering of striated muscles. *Ann Biomed Eng* 42(7):1391–1405.
25. Liao I-C, Liu JB, Bursac N, Leong KW (2008) Effect of Electromechanical Stimulation on the Maturation of Myotubes on Aligned Electrospun Fibers. *Cell Mol Bioeng* 1(2-3): 133–145.
26. Macklem PT (2008) Emergent phenomena and the secrets of life. *J Appl Physiol (1985)* 104(6):1844–1846.

Supporting Information

Raman et al. 10.1073/pnas.1516139113

SI Methods

Cell Infection and Culture. C2C12 murine myoblasts were infected with pLenti2-EF1α-ChR2[H134R]-tdTomato-WPRE plasmid to express a mutated variant of the light-sensitive ion channel, Channelrhodopsin (ChR2[H134R]). The tdTomato tag was used to selectively enrich myoblasts that expressed ChR2[H134R] via FACS. Cells were maintained in growth medium (GM) consisting of DMEM with L-glutamine and sodium pyruvate (Corning Cellgro) supplemented with 10% (vol/vol) FBS (Lonza), 1% (vol/vol) L-glutamine (Cellgro Mediatech), and 1% (vol/vol) penicillin-streptomycin (Cellgro Mediatech).

Design and Fabrication of Flexible 3D Printed Bio-Bot Skeletons. A commercial stereolithographic 3D printing apparatus (SLA 250/50; 3D Systems) was used to manufacture parts designed in CAD software (Solidworks) and sliced into printed layers by 3D Lightyear software (v1.4; 3D Systems). The injection molds were fabricated on glass slides using a prepolymer solution composed of 20% (wt/vol) PEGDMA MW 1,000 g/mol (Polysciences) in PBS (Lonza) with 0.5% (wt/vol) 1-[4-(2-hydroxyethoxy)phenyl]-2-hydroxy-2-methyl-1-propanone-1-one photoinitiator (Irgacure 2959; BASF) dissolved in DMSO (Fisher Scientific). The bio-bot skeletons were fabricated on glass slides using a prepolymer solution composed of 20% (vol/vol) PEGDA MW 700 g/mol (Sigma-Aldrich) in PBS with 0.5% (wt/vol) Irgacure 2959 photoinitiator dissolved in DMSO. Following fabrication, molds and bio-bot skeletons were rinsed in PBS, sterilized in 100% ethanol (Decon Labs) for 1 h, and stored in PBS for at least 1 h before use. For parts that required chemical tethering to the underlying slides, the glass was pretreated with 2% (vol/vol) 3-(trimethoxysilyl) propyl methacrylate (Sigma-Aldrich) in 100% ethanol for 5 min, washed in 100% ethanol for 5 min, and baked at 110 °C for 3 min.

Formation of Optogenetic Muscle Rings and Strips. Strip molds were assembled by placing bio-bot skeletons within holders. Both strip molds and ring molds were kept moist, but unsubmerged, in PBS during the injection molding process. Optogenetic C2C12 myoblasts were trypsinized (TrypLE; Life Technologies), suspended in a solution of GM supplemented with 1 mg/mL ACA (Sigma Aldrich) (GM+), and combined with ice cold 30% (vol/vol) Matrigel basement membrane matrix (BD Biosciences), 4 mg/mL fibrinogen (Sigma-Aldrich), and 0.5 U/mg-fibrinogen thrombin (Sigma-Aldrich) for a total cell/gel solution volume of 120 μL per muscle strip or ring. This cell/gel solution was immediately injected into the strip/ring molds and incubated at 37 °C for 1 h before the addition of enough GM+ to submerge the muscle. The muscle actuators were then incubated for 3 d in GM+, with daily media changes, and incubated after that in differentiation medium (DM++) with daily media changes. The differentiation medium consisted of DMEM with L-glutamine and sodium pyruvate (Corning Cellgro), supplemented with 10% (vol/vol) heat inactivated HS (Lonza), 1% (vol/vol) L-glutamine, 1% (vol/vol) penicillin-streptomycin, 1 mg/mL ACA, and 50 ng/mL IGF1 (Sigma-Aldrich).

Optical and Electrical Stimulation. Muscle strip and ring actuators were optically stimulated using a 470-nm LED (Mightex). Trains of 50-ms pulses of specified frequency (1, 2, and 4 Hz) were generated using a custom-built device. The LED output was focused using a lens, and a maximum power of 1.9 mW/mm^2 was used (corresponding to a spot diameter of 8 mm). Optical stimulation of bio-bots was conducted in DM++ media, and all movies were taken through a red camera filter to make the focused nature of the light stimulus easier to visualize. During exercise training, a 2-min rest period was incorporated between stimulation at different frequencies, and all experiments were performed at 37 °C. Electrical stimulation was conducted using a custom-built electrical setup designed to provide bipolar electrical pulses of 20-V amplitude (21.6 V/cm field strength) and 50-ms pulse width, as previously described (10). Electrical stimulation of bio-bots was conducted in serum-free DMEM to reduce electrolysis.

Measurement of Force Production and Locomotive Speed. Passive tension force was measured by correlating the deflection of the curved beam in the bio-bot skeleton to the contractile force applied on the bio-bot skeleton's pillars. Displacements were measured in ImageJ (National Institutes of Health), and passive tension force was calculated from an equation derived from Euler-Bernoulli beam-bending theory: $P = (8EI/lL^2)\delta_{max}$. In this equation, E represents the Young's modulus of the beam (319 kPa) as measured using a tensile mechanical testing apparatus. I is the moment of inertia, L is the beam length, l is the measured moment arm from the muscle strip to the beam, and δ_{max} is the measured beam deflection. Active tension force was measured by correlating the displacement of the ends of the bio-bot skeleton to the active contractile force produced in response to an external stimulus. The bio-bot was treated as a Kelvin-Voigt viscoelastic structure composed of a spring and damper in parallel, where applied stresses are related to measured strains by the following equation: $\sigma(t) = E\varepsilon(t) + \eta[d\varepsilon(t)/dt]$, as previously described (10). Speed was calculated by dividing distance traveled by time.

Immunofluorescence Imaging. Muscle strips and rings were rinsed in PBS, fixed in 4% (vol/vol) paraformaldehyde (EMD Chemicals) for 30 min, permeabilized with 0.2% (vol/vol) Triton X-100 (Sigma-Aldrich) for 10 min, and stored in blocking solution (Image-iT FX Signal Enhancer; Invitrogen) before staining. The muscle was then incubated in mouse MF-20 antimyosin heavy chain (1:400 dilution in Image-iT FX, Developmental Studies Hybridoma Bank, The University of Iowa Department of Biology) for 6 h at 4 °C. They were then incubated with Alexa Fluor 488 goat anti-mouse IgG secondary antibody (1:400 dilution in Image-iT FX; Invitrogen) for 12 h at 4 °C. Next, they were incubated in DAPI (1:5,000 in sterilized deionized water; Sigma-Aldrich) for 10 min before fixation onto a glass-bottom dish (MatTek) with warm agarose gel and imaging with a confocal microscope (LSM 710; Zeiss).

DNA/Protein Quantification. Muscle rings were detached from hydrogel skeletons, rinsed in PBS, and snap frozen in liquid nitrogen before storage at −80 °C. At the time of analysis, rings were weighed, halved, and weighed again. The DNA concentration in each half was measured using a spectrophotometer (NanoDrop 1000) at 260 nm after genomic DNA was isolated using a DNeasy Blood and Tissue Kit (Qiagen). Total DNA content was calculated from the concentration using the known elution volume and total muscle ring mass. The other halves of the muscle rings were lysed in RIPA buffer (Thermo Scientific) on ice and briefly sonicated (Digital Sonifier 150; Branson). Cells were centrifuged, and the supernatant was collected and diluted. Protein concentration in these halves was determined with a spectrophotometer by comparing absorbance of each sample at 562 nm to a standard curve of BSA protein absorbance vs.

concentration, using a Pierce BCA Protein Assay Kit (Thermo Scientific). Total protein content was calculated from the concentration using known supernatant volume and total muscle ring mass.

Statistical Analysis. Statistical analysis was performed via one-way ANOVA followed by Tukey's multiple comparison test for $P < 0.05$ using OriginPro software. Results are presented as mean ± SD.

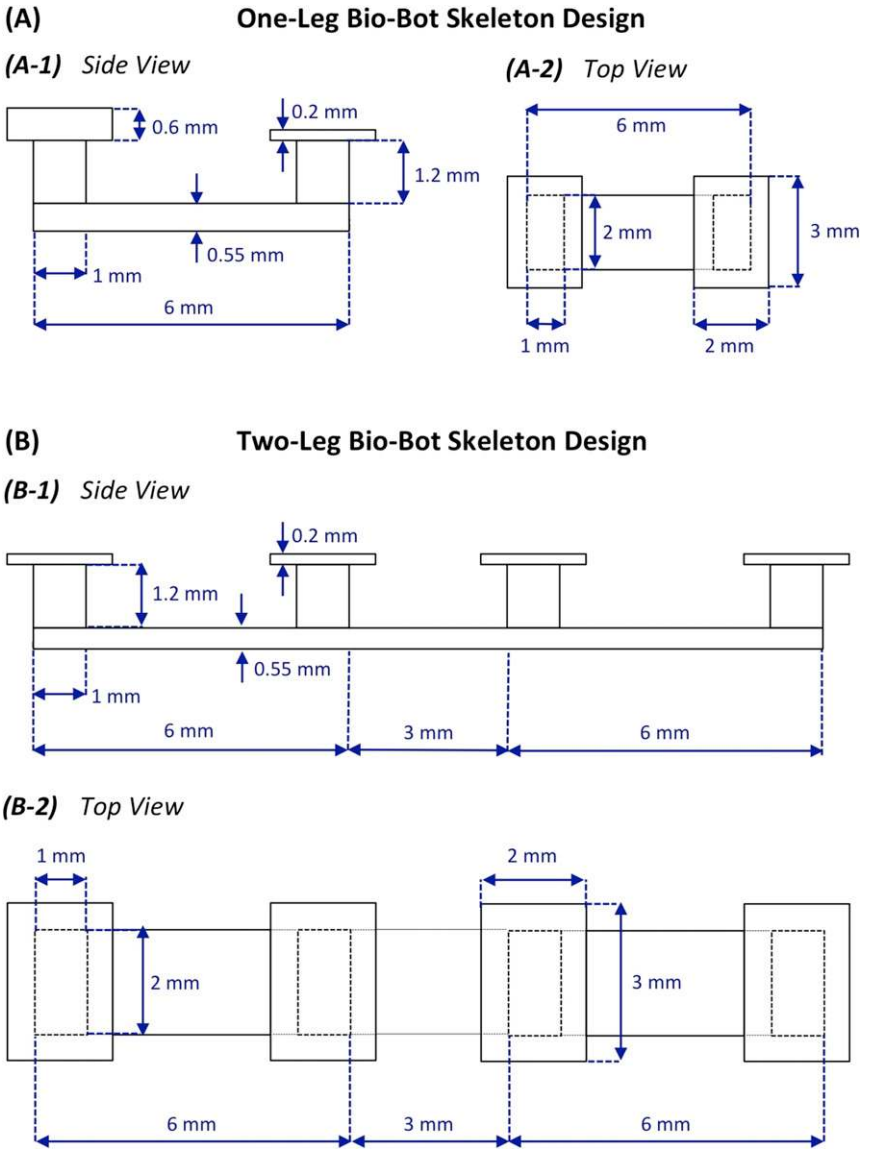

Fig. S1. (*A*) Design dimensions for asymmetric one-leg bio-bot skeletons shown as side view (*A-1*) and top view (*A-2*) schematics. (*B*) Design dimensions for symmetric two-leg bio-bot skeletons shown as side view (*B-1*) and top view (*B-2*) schematics.

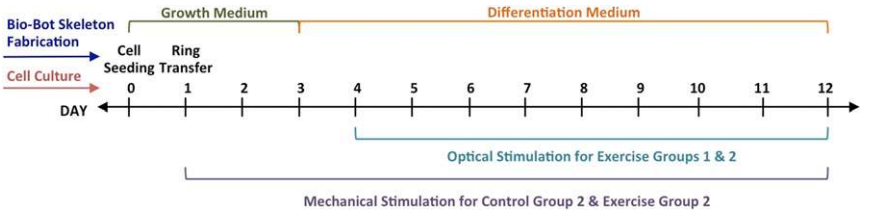

Fig. S2. Schematic showing timeline of growth, differentiation, and exercise training of tissue engineered modular muscle ring actuators.

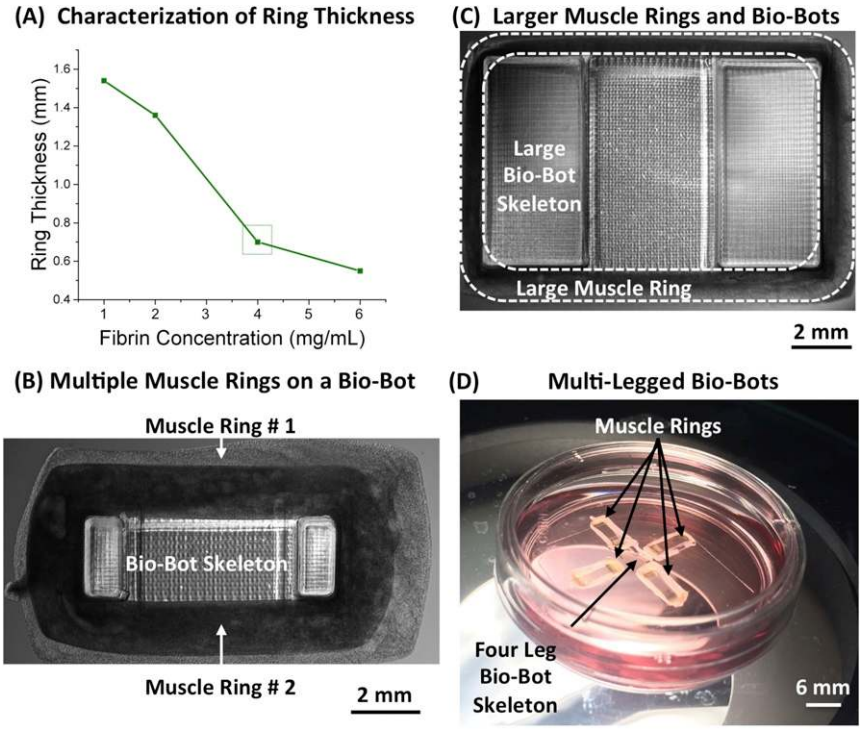

Fig. S3. (*A*) Characterization of ring thickness as a function of fibrin concentration. A concentration of 4 mg/mL was chosen for its ability to generate compact muscle strips with high cellular density. Higher concentrations than this resulted in marginal changes in muscle strip thickness. (*B*) The dimensions of rings can be readily modified to power larger-scale bio-bot structures by adjusting the volume of the cell/gel solution. This ring was formed from 240 μL cell/gel solution, compared with those used in the study, which were formed from 120 μL cell/gel solution. (*C*) The modularity of the muscle ring actuator design allows for the addition of multiple muscle rings per device, providing an added mechanism of improving functional performance of bio-integrated machines and systems in the future. (*D*) The modularity of the muscle ring actuator design also enables the fabrication of multilegged bio-bot structures, such as the "four-leg" bio-bot shown here. Because directional locomotion and 2D steering proved to be achievable even with two-leg structures, only data for two-leg structures were presented in this study.

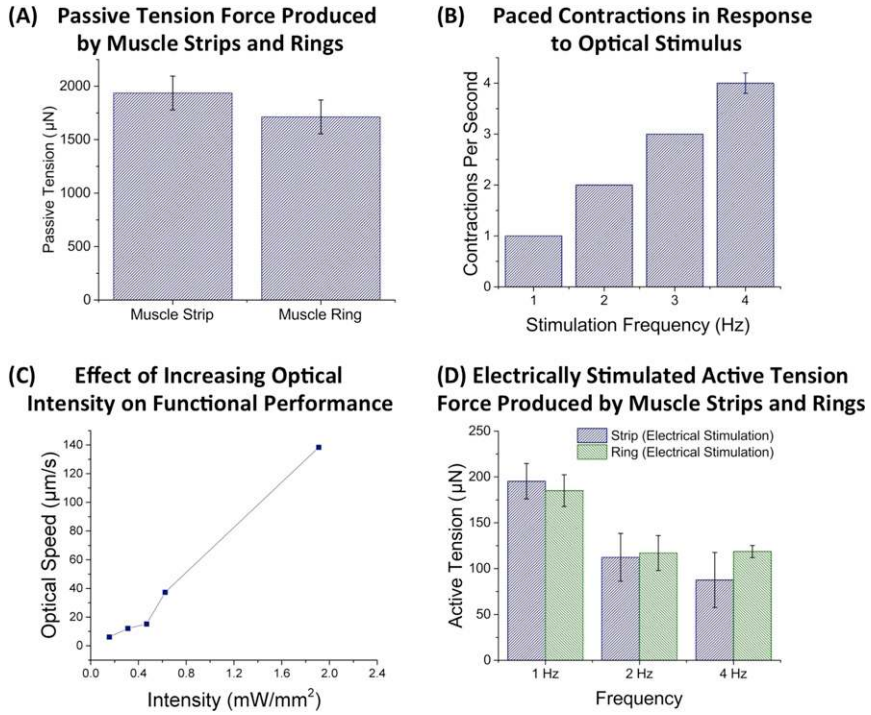

Fig. S4. (*A*) Passive tension force produced by muscle strips and muscle rings. There is no significant difference between the passive tension forces produced by muscle strips and rings ($P < 0.05$, $n = 9$, one-way ANOVA, post hoc Tukey test). (*B*) Optogenetic muscle rings produced paced contractions in response to optical stimulus at frequencies from 1 to 4 Hz. Muscle rings tested at higher-frequency stimulations produced paced contractions until a tetanus frequency above 8–10 Hz ($n = 4$). (*C*) Effect of increasing optical intensity on the directional locomotive speed of optically stimulated asymmetric one-leg bio-bots. A maximum energy density of 1.9 mW/mm^2 was used for all experiments presented in this study. (*D*) Active tension force produced by muscle strips and rings in response to electrical stimulation reveals that electrical stimulation produces comparable contractile forces for both actuator designs ($P < 0.05$, $n = 3$, one-way ANOVA, post hoc Tukey test).

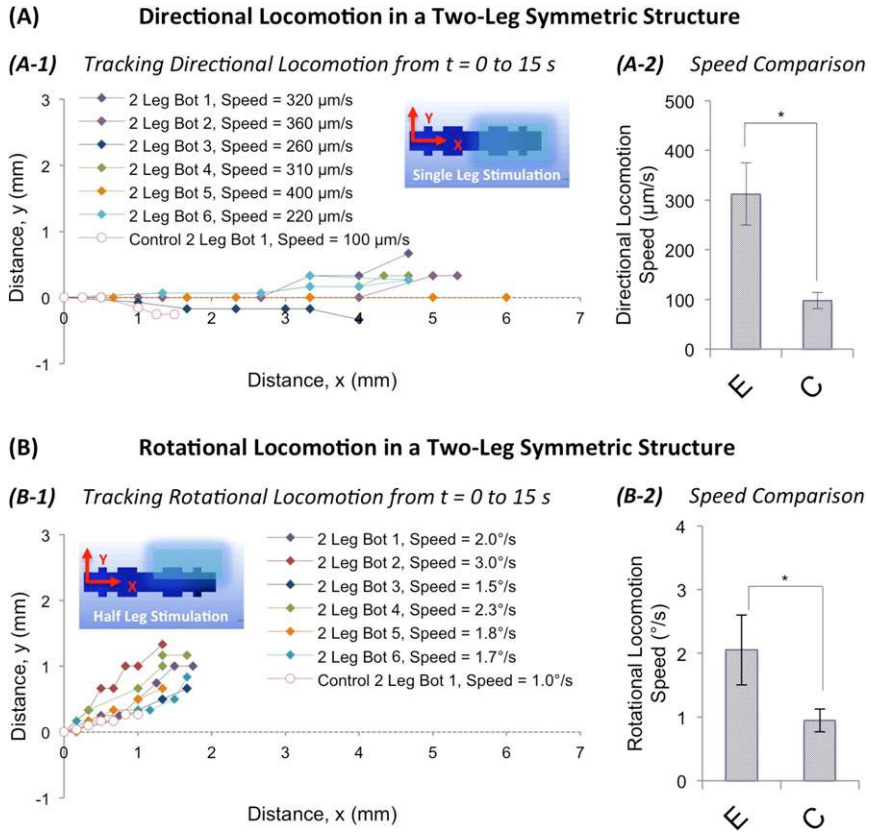

Fig. S5. (*A*) Directional locomotion in response to single-leg stimulation of two-legged bio-bots. (*A-1*) X-Y tracking of top-view movies of bio-bots over 15 s at 2-Hz optical stimulation. Average locomotive speed for exercise group 2 bio-bots is 312 ± 63 μm/s. Devices also demonstrated small rotations under full-ring stimulation, with an average speed of 0.24 ± 0.1°/s. (*A-2*) Comparison of directional locomotive speed in response to optical stimulation at 2 Hz for exercise group 2 bio-bots (labeled E) ($n = 6$) and control group 2 bio-bots (labeled C) ($n = 3$). Exercised bio-bots demonstrate significantly higher locomotive speeds than control bio-bots ($P < 0.05$, one-way ANOVA, post hoc Tukey test). (*B*) Rotational locomotion in response to half-leg stimulation of two-legged bio-bots. (*B-1*) X-Y tracking of top-view movies of the same bio-bots presented in *A-1* over 15 s at 2-Hz optical stimulation. Average rotational speed for exercise group 2 bio-bots is 2.1 ± 0.5°/s. Devices also small translocations under full-ring stimulation, with an average speed of 33 ± 10 μm/s. (*B-2*) Comparison of rotational locomotive speed in response to optical stimulation at 2 Hz for exercise group 2 bio-bots (labeled E) ($n = 6$) and control group 2 bio-bots (labeled C) ($n = 3$). Exercised bio-bots demonstrate significantly higher locomotive speeds than control bio-bots ($P < 0.05$, one-way ANOVA, post hoc Tukey test).

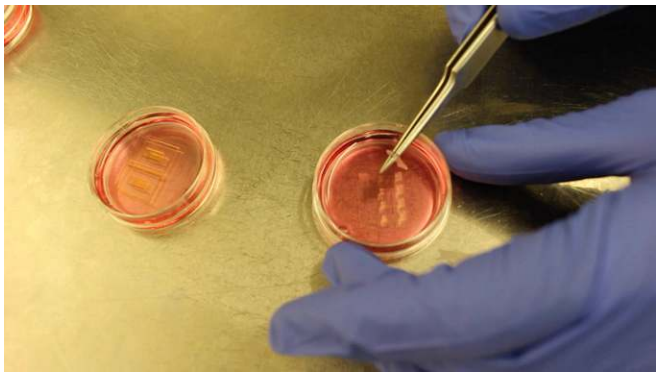

Movie S1. Manual transfer of muscle ring from injection mold to bio-bot skeleton. Muscle rings are lifted from the injection mold using sterile tweezers and transferred to another dish containing the bio-bot skeletons (chemically bonded to an underlying glass slide). The muscle ring is tethered around the bio-bot skeleton on day 1 after seeding.

Movie S1

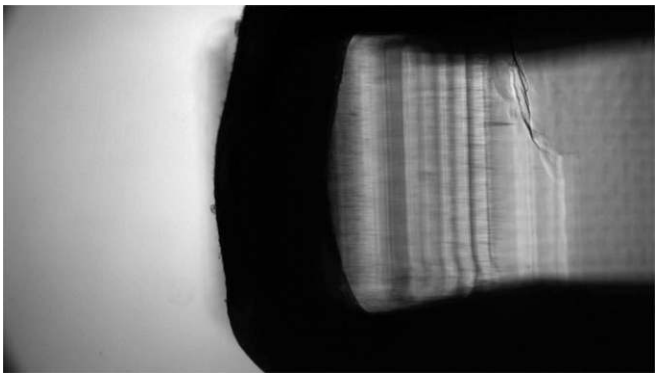

Movie S2. Optical stimulation of muscle rings in exercise study. Active tension force output in response to optical stimulation is calculated using a Kelvin-Voigt viscoelasticity model that relates bio-bot skeleton deformation to muscle force produced. Numerical results are presented in Fig. 4*B*.

Movie S2

Movie S3. Directional locomotion of muscle ring-powered bio-bot with asymmetric geometry. Optical stimulation (at 2 Hz) of a muscle ring tethered to a bio-bot with asymmetric geometry leads to directional locomotion in the direction of the longer pillar. Numerical results and speed-frequency response are presented in Fig. 5.

Movie S3

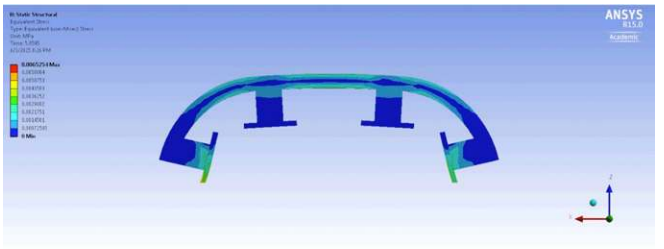

Movie S4. Zero net locomotion in muscle ring-powered bio-bot with symmetric geometry (FEA). FEA simulation of electrically stimulated actuation of both muscle rings in a bio-bot with symmetric geometry. Due to overall symmetry of both geometry and force production, the bio-bot demonstrates zero net locomotion.

Movie S4

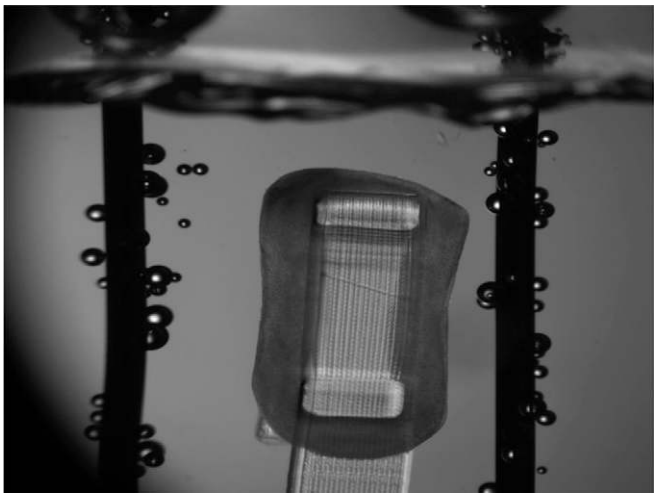

Movie S5. Zero net locomotion in muscle ring-powered bio-bot with symmetric geometry (electrical stimulation). Electrically stimulated actuation (at 2 Hz) of both muscle rings in a bio-bot with symmetric geometry. Due to overall symmetry of both geometry and force production, the bio-bot demonstrates zero net locomotion.

Movie S5

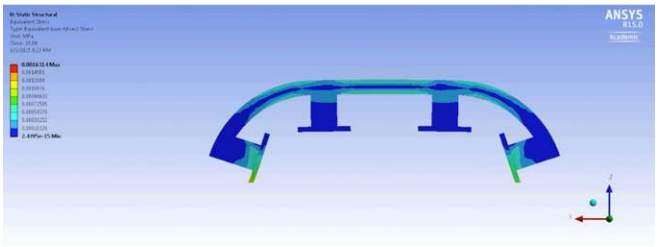

Movie S6. Directional locomotion in muscle ring-powered bio-bot with symmetric geometry (FEA). FEA simulation of targeted optically stimulated actuation of one muscle ring in a bio-bot with symmetric geometry. Despite overall symmetry of geometry, the asymmetry in force production causes greater contractile displacement in the stimulated leg (right leg), driving locomotion toward the right.

Movie S6

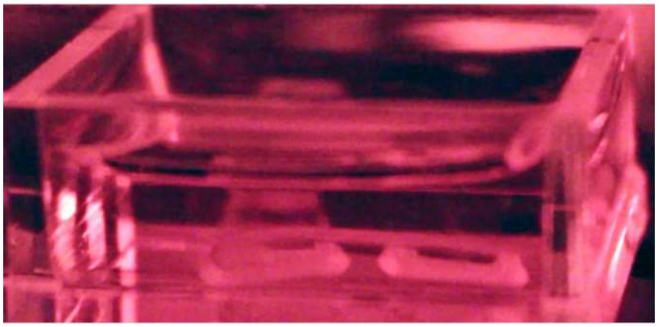

Movie S7. Directional locomotion in muscle ring-powered bio-bot with symmetric geometry (optical stimulation). Targeted optically stimulated actuation (at 2 Hz) of one muscle ring in a bio-bot with symmetric geometry. Despite overall symmetry of geometry, the asymmetry in force production causes greater contractile displacement in the stimulated leg (right leg), driving locomotion toward the right.

Movie S7

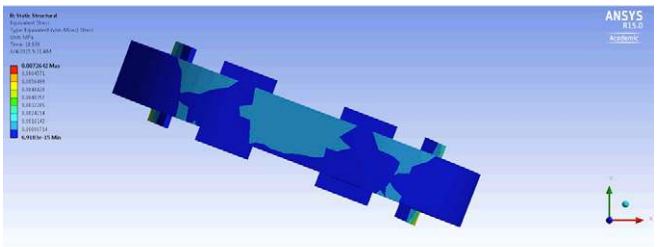

Movie S8. Rotational locomotion in muscle ring-powered bio-bot with symmetric geometry (FEA). FEA simulation of targeted optically stimulated actuation of one half of a muscle ring in a bio-bot with symmetric geometry. Despite overall symmetry of geometry, the asymmetry in force production causes greater contractile displacement in one part of the partially stimulated leg (bottom right leg), driving clockwise rotational locomotion in the direction of the stimulated leg.

Movie S8

Movie S9. Rotational locomotion in muscle ring-powered bio-bot with symmetric geometry (optical stimulation). Targeted optically stimulated actuation (at 2 Hz) of one half of a muscle ring in a bio-bot with symmetric geometry. Despite overall symmetry of geometry, the asymmetry in force production causes greater contractile displacement in one part of the partially stimulated leg, driving clockwise rotational locomotion in the direction of the stimulated leg. The focal spot of the LED was precisely positioned on the right half of the muscle ring furthest away from the camera, which saturates the light signal due to the high intensity of the light stimulus.

Movie S9

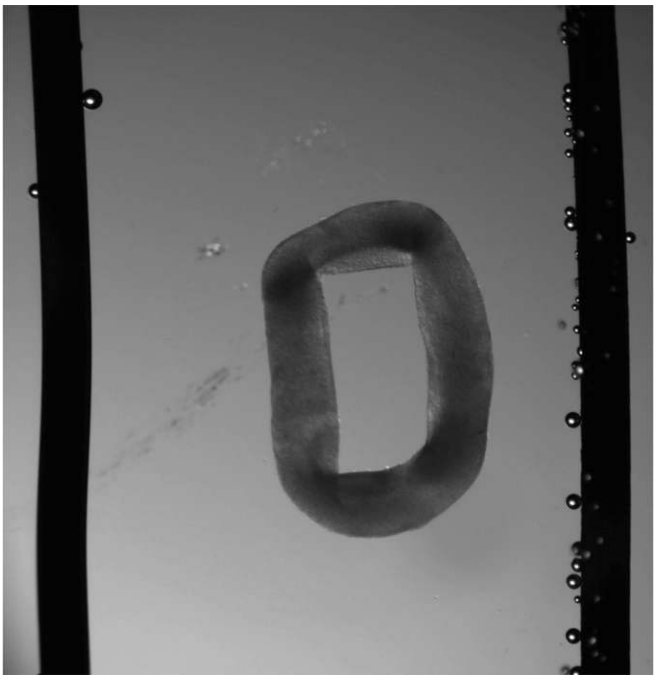

Movie S10. Electrical stimulation of untethered muscle ring actuator. Muscle rings produce significant contractile force even when untethered to a mechanical skeleton, as demonstrated here in response to electrical stimulation (2 Hz) on day 12 after seeding. These muscle rings were maintained in the injection mold throughout the growth and differentiation processes. In this movie, some net locomotion of the ring is observed, but directionality is not controlled. Coupling the modular ring to a forward-engineered 3D printed skeleton would enable controllable directional locomotion.

Movie S10